Journal of the Mechanics and Physics of Solids 135 (2020) 103784

Contents lists available at ScienceDirect

Journal of the Mechanics and Physics of Solids

journal homepage: www.elsevier.com/locate/jmps

# Optimal quantum valley Hall insulators by rationally engineering Berry curvature and band structure

Zongliang Du[1], Hui Chen[1], Guoliang Huang*

*Department of Mechanical and Aerospace Engineering, University of Missouri, Columbia, Missouri 65211, USA*

ARTICLE INFO

*Article history:*
Received 18 August 2019
Revised 1 November 2019
Accepted 10 November 2019
Available online 12 November 2019

*Keywords:*
Optimal valley Hall insulators
Systematic design
Explicit geometry description
Band structure and Berry curvature engineering

ABSTRACT

We propose the concept of "optimal quantum valley Hall insulators" and formulate it to an optimization formulation. In this new design paradigm, mechanical valley Hall insulators with simple geometries, large relative operating bandwidths and highly localized interface modes can be obtained in a systematic way. Compared to existing classical work based trail-and-error method via breaking symmetry, advantages of the new strategy are: (1) it simultaneously confines the Berry curvature and tailors the band structure to achieve robustness and optimality; (2) it adopts an explicit structural optimization method to describe and optimize the unit cells with a few design variables, which paves a rational way to explore a relatively large design space efficiently; (3) valley Hall insulators with quite different geometries and a better performance can be produced directly through an optimization process without introducing and manually tuning the unit cell with Dirac cone feature. This methodology can not only be easily extended to design optimized topological insulators in other physical systems, but also provides some insight into optimization aided band structure and Berry curvature engineering.



## 1. Introduction

Topological insulators (TIs), which are fundamentally built on the topological states or topological invariants in condensed matter physics (Berry, 1984; Simon, 1983; Thouless et al., 1982), provided a new paradigm for designing devices with improved functionalities (Hasan and Kane, 2010; Qi and Zhang, 2011). Inspired by the incredible ability of supplying a topologically-protected energy transport with an extremely high transmission rate and immunity to backscattering, significant research interest has been devoted to design and test TIs in other physical systems, e.g., photonics (Khanikaev et al., 2013; Kitagawa et al., 2011; Lu et al., 2016b; Ozawa et al., 2019; Wang et al., 2009) and acoustics (He et al., 2016; 2018; Lu et al., 2014; Ma et al., 2019; Xia et al., 2018), among others. For mechanical systems, to bridge the gap between quantum topological theory and classical mechanics, a recent study provided fundamental and physical interpretation on interfacial wave propagation in the mechanical TIs from continuum mechanics perspective (Chen et al., 2018a). As an analogue of the quantum Hall effect, mechanical quantum Hall insulators have been proposed and result protected one-way elastic edge waves unaffected by disorders utilizing Coriolis force (Wang et al., 2015b), or gyroscopic coupling (Nash et al., 2015; Wang et al., 2015a), or time-modulated properties (Chen et al., 2019a). Besides, quantum spin Hall effect has also been extended to mechanical systems both theoretically (Chen et al., 2018b; Huo et al., 2018; Mousavi et al., 2015) and experimentally

* Corresponding author.
*E-mail address:* huangg@missouri.edu (G. Huang).
[1] These authors contributed equally

https://doi.org/10.1016/j.jmps.2019.103784
0022-5096/

(Miniaci et al., 2018; Süsstrunk and Huber, 2015; Yu et al., 2018) by applying zone-folding strategy. Not requiring external inputs or gyroscopic materials or strong spin-orbit couplings, quantum valley Hall effect appears at two inequivalent valleys carrying distinct valley characteristics and can be generally achieved by breaking inversion symmetry (Rycerz et al., 2007; Xiao et al., 2007). The corresponding mechanical analogues were developed both for out-of-plane (Pal and Ruzzene, 2017) and in-plane cases (Chen et al., 2018a) with experimental demonstrations (Meeussen et al., 2016; Vila et al., 2017; Yan et al., 2018). Enjoying the topologically-protected properties, all those three classes of mechanical TIs could have useful applications in waveguides and devices for vibration isolation/confinement, impact mitigation and the transfer of information through elastic waves (Liu et al., 2019; Ma et al., 2019; Pal and Ruzzene, 2017; Yan et al., 2018).

Based on the theoretical principle of electron TIs, for designing valley Hall insulators, a trail-and-error procedure is commonly used in literature through manually tuning the unit cells (UCs) as: (1) finding a UC with Dirac cone feature at high symmetry points; (2) splitting the Dirac cone by breaking the mirror or inversion symmetry of the base UC; (3) verifying the quantum valley Hall effect of the designs. Following such procedure, quantum valley Hall insulators have been designed successfully in some degree and validated in various fields such as photonics (Dong et al., 2017; Gao et al., 2018; Kang et al., 2018; Noh et al., 2018), acoustics (He et al., 2018; Lu et al., 2016a; 2017; Xia et al., 2019; Zhang et al., 2018) and mechanics (Chen et al., 2018a; Lu et al., 2018; Pal and Ruzzene, 2017; Vila et al., 2017; Yan et al., 2018), among others. In the continuum media, some regular-shaped holes, e.g., circulars and regular triangles, are always adopted as basic components for tuning hexagonal UCs. By rotating a regular triangle void inside, representative designs proposed for phononic crystals (Lu et al., 2016a; 2014), have been experimentally verified (Lu et al., 2017; Yan et al., 2018) recently.

It should be noted that, for practical applications, TIs with simple geometries, wide operating bandwidth, highly localized interface modes, which lead to the concept of "optimal design", are highly desired. However, to the best of our knowledge, most of the investigations on designing valley Hall insulators focus on the realization of topological phenomena in different physical systems through the aforementioned intuitive procedure. In addition, depending on the preknowledge and intuition of designers, the traditional design procedure has some limitations: (1) the design space, e.g., regular-shaped holes, is substantially limited for geometry selection; (2) by manually breaking symmetry, the Hall insulator pairs with a similar geometry cannot achieve the widest operating bandwidth; (3) the trail-and-error procedure lacks guarantee of mathematical optimality. Lately, inverse design method has been adopted to design UCs with two-fold (Nanthakumar et al., 2019) and four-fold Dirac degeneracy (Chen et al., 2019b) for enhancing the traditional design procedure of spin Hall insulators. Besides, by innovatively optimizing the directional field propagating along a well-selected waveguide, spin Hall insulators for acoustics and photonics were successfully obtained for some specific frequencies via topology optimization (Christiansen et al., 2019a; 2019b). To study the electromagnetic realization of valley Chern effect, Prodan and his coworkers introduced an alternating current circuitry of *LC* resonators to reproduce the Hamiltonian driving the electrons in graphene (Eisenberg et al., 2019). They managed to achieve a high *Q* factor by optimizing the circuit configuration. Nevertheless, systematic design method of optimized valley Hall insulators is far from mature.

In the present work, the Moving Morphable Void method is modified to describe the UCs in a relatively large design space with only a few design variables (Zhang et al., 2017b). By introducing some quantitative gauges, alternative strategies are developed for inverse design of valley Hall insulators based on the ideas of achieving band inversion and maximizing the width of common bandgap. Based on them, to guarantee the topological robustness and transport performance, the concept of "optimal quantum valley Hall insulators" is proposed and formulated into an optimization formulation to rationally engineer the Berry curvature and band structure. The performance of the optimized insulators is verified as compared to a representative design in literature (Lu et al., 2016a; 2014), showing a significantly increased relative operating bandwidth and a better transport of elastic wave.

The rest of this paper is organized as follows: a novel geometry description method for continuum UCs with specific symmetries is presented in Section 2, followed by the band structure analysis and Berry curvature analysis of mechanical valley Hall insulators in Section 3; by introducing some quantitative measures, two elementary inverse design methods are developed in Section 4; then the advanced strategy to obtain "optimal quantum Valley Hall insulators" is proposed and verified in Section 5 by comparing with a reference design in literature; conclusion and discussion are contained in the last section.

## 2. A novel geometry description method for continuum UCs with specific symmetries

Topology optimization has been successfully used for the systematic design of metamaterials (Jensen and Sigmund, 2011; Li et al., 2019; Molesky et al., 2018). Among the popular topology optimization methods (Bendsøe and Sigmund, 2004; Guo et al., 2014; Wang et al., 2003; Xie and Steven, 1993), we adopted Moving Morphable Void (MMV) method (Xue et al., 2019; Zhang et al., 2017b) to describe the UCs with specific symmetries by restricting the symmetry of the void in the UCs. Moreover, the highly reduced number of design variables would be beneficial when gradient-free algorithms, e.g., Genetic Algorithm (GA), are used.

### 2.1. Modified moving morphable void (MMV) method

In the MMV topology optimization method (Xue et al., 2019; Zhang et al., 2017b), the void region in a design domain is composed by a set of voids, and each void is described as a B-spline through a well-constructed manner to avoid self-

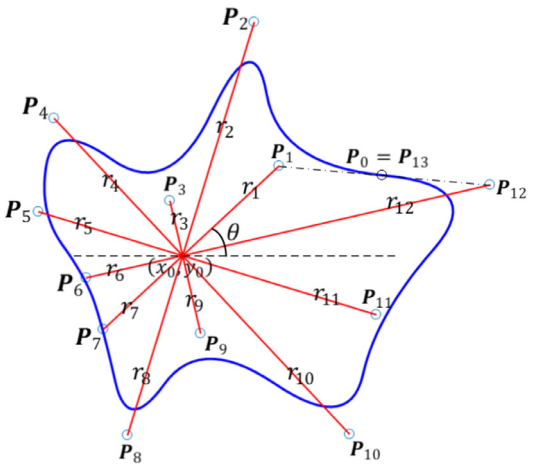


**Fig. 1.** An illustration of a single void described by a B-spline in the modified MMV method.

intersection. By optimizing locations and shapes of the distributed voids in the design domain, optimized designs can be obtained.

As illustrated in Fig. 1, in the modified MMV method, a reference angle is introduced to further improve the deformability of each single void. In this manner, determined by the central point, a set of control points and a reference angle, each void can be explicitly described by a B-spline formulated as:

$$\boldsymbol{C}(u) = \sum_{i=0}^{n+1} N_{i,2}(u)\boldsymbol{P}_i, \quad (0 \le u \le 1) \tag{1}$$

with $n$ denoting the total number of control points $\boldsymbol{P}_i$ ($n = 12$ in Fig. 1), which are expressed as:

$$\boldsymbol{P}_k = \begin{cases} \left(x_0 + r_k \cos\left((k-1)\dfrac{2\pi}{n} + \theta\right), y_0 + r_k \sin\left((k-1)\dfrac{2\pi}{n} + \theta\right)\right)^\top & \text{if } k = 1, \ldots, n \\ \dfrac{\boldsymbol{P}_1 + \boldsymbol{P}_{n-1}}{2} & \text{if } k = 0 \text{ or } n+1 \end{cases} \tag{2}$$

with $(x_0, y_0)$ denoting the coordinate of the central point, $r_1, \ldots, r_n$ denoting the distances from the control points to the central point and $\theta$ denoting the reference angle between the horizontal line to the line along the central point and $\boldsymbol{P}_1$, respectively. In addition, $N_{i,2}(u)$ is the second order B-spline basis function generated by a knot vector $U = (u_0, u_1, \ldots, u_{n+4})$ with $0 \le u_0 \le u_1 \le \ldots \le u_{n+4} \le 1$ through the following recursive way:

$$N_{i,k}(u) = \frac{u - u_i}{u_{i+k} - u_i} N_{i,k-1}(u) + \frac{u_{i+k+1} - u}{u_{i+k+1} - u_{i+1}} N_{i+1,k-1}(u), k \ge 1 \tag{3}$$

and

$$N_{i,0} = \begin{cases} 1, & \text{if } u_i \le u < u_{i+1} \\ 0, & \text{otherwise} \end{cases} \tag{4}$$

Therefore, the B-spline described void in modified MMV method can be determined by a design vector $\boldsymbol{D} = (x_0, y_0, r_1, \ldots, r_n, \theta)^\top$ explicitly.

### *2.2. Geometry description of continuum UCs with specific symmetries by the modified MMV method*

In the present work, for simplicity, only the out-of-plane degree of freedom of two-dimensional hexagonal UCs with a unit thickness is considered. In addition, the adopted parameters are: lattice vector $a = \sqrt{3}$ cm, Young's modulus $E = 69.0$ GPa, Possion's ratio $\nu = 0.35$ and density $\rho = 2.7 \times 10^3$ kg/m$^3$.

Topology optimization method has exceptional ability to systematically design highly efficient structures/materials with very complex geometry (Bendsøe and Sigmund, 2004; Jensen and Sigmund, 2011; Li et al., 2019). In the present work, taking the requirement of simple geometry into consideration, we assume the desired valley Hall insulators are hexagons with only one void inside, as the reference designs with a triangular void (Lu et al., 2016a; 2014). We refer the interested readers to some previous work (Bendsøe and Sigmund, 2004; Jensen and Sigmund, 2011; Li et al., 2019) for eigenvalue analysis related topology optimization with multiple holes and topology change.

Taking the advantage of uniform distribution of control points along circumferential angle, UCs with specific symmetries can be easily described using the modified MMV method. For instance, for the case with 12 control points, by locating the

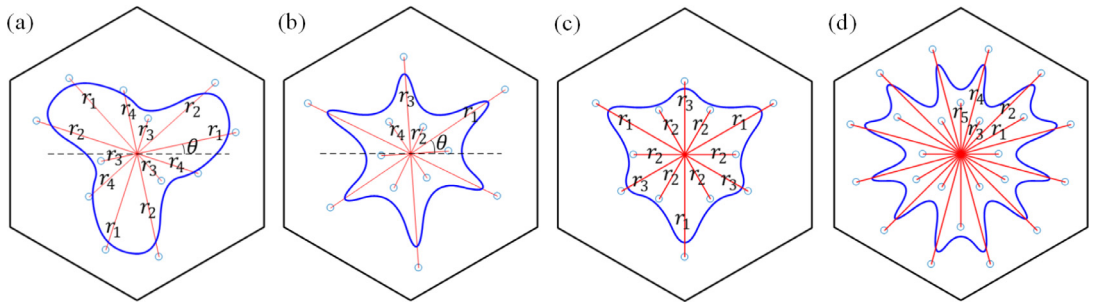


**Fig. 2.** Description of insulators using the modified MMV method: (a) a $C_3$-symmetric UC with $\boldsymbol{D} = (0.69\text{cm}, 0.72\text{cm}, 0.25\text{cm}, 0.44\text{cm}, 12^\circ)^\top$ (b) a $C_3$-symmetric UC with $\boldsymbol{D} = (0.78\text{cm}, 0.20\text{cm}, 0.66\text{cm}, 0.26\text{cm}, 38^\circ)^\top$ (c) a $C_{3v}$-symmetric UC described by 12 control points and 3 design variables (d) a $C_{3v}$-symmetric UC described by 24 control points and 5 design variables.

central point at the center of UCs, we only need 5 design variables, i.e., $\boldsymbol{D} = (r_1, r_2, r_3, r_4, \theta)^\top$, to characterize a large set of $C_3$-symmetric hexagonal UCs, such as the two examples with quite different geometries illustrated in Fig. 2(a,b). For a $C_{3v}$ symmetric UC, the design variable vector can be simplified to $\boldsymbol{D} = (r_1, r_2, r_3)^\top$ as Fig. 2(c), i.e., by locating the central point at the center of UC while setting $r_1 = r_5 = r_9, r_2 = r_4 = r_6 = \ldots = r_{12}, r_3 = r_7 = r_{11}$ and $\theta = 0$. More complex shapes can be described by introducing more control points in a similar way. As shown in Fig. 2(d), for instance, adopting 24 control points, $\boldsymbol{D} = (r_1, r_2, \ldots, r_5)^\top$ is able to describe a more complex UC-set with $C_{3v}$ symmetry. In this manner, a relatively large design space of UCs with specific symmetries can be described by using only a few design variables.

## 3. Band structure and Berry curvature analysis of continuum mechanical valley Hall insulators

### 3.1. Band structure analysis

Wave propagation in an isotropic homogeneous elastic solid is governed by:

$$\rho\ddot{u} = \lambda\nabla(\nabla\cdot u) + \mu\nabla\cdot(\nabla u + u\nabla), \qquad u(\boldsymbol{x}, t) \in \mathcal{U}_{\text{ad}} \tag{5}$$

where $\lambda$, $\mu$ denote the Lamé coefficients and $\rho$ is the density of the material (see, e.g., (Achenbach, 2012)). The symbols $\nabla$ and $u$ are the gradient operator and the out-of-plane displacement field belonging to its admissible space $\mathcal{U}_{\text{ad}}$.

Finite element method is commonly adopted to solve the governing Eq. (5) to analyze the dynamic behavior of UCs. During numerical implementation, a fixed Cartesian mesh and quadrilateral elements are adopted. The elemental stiffness matrix and elemental mass matrix are interpolated using the ersatz material model as Zhang et al. (2017b, 2016):

$$\mathbf{k}_e = \rho_e\mathbf{k}_0, \quad \mathbf{m}_e = \rho_e\mathbf{m}_0 \tag{6}$$

where $\rho_e$ is the area fraction of $e$-th element determined for each intermediate design and $\mathbf{k}_0$, $\mathbf{m}_0$ are elemental stiffness matrix, elemental mass matrix available in textbooks, e.g., Hughes (2012).

According to Floquet-Bloch boundary condition (Kittel et al., 1996), the condensed stiffness matrix and condensed mass matrix can be calculated as

$$\mathbf{K} = \mathbf{G}^{\text{H}}\mathbf{K}^0\mathbf{G}, \quad \mathbf{M} = \mathbf{G}^{\text{H}}\mathbf{M}^0\mathbf{G} \tag{7}$$

where $\mathbf{K}^0$ and $\mathbf{M}^0$ are the global stiffness matrix and global mass matrix assembled using the elemental matrices in Eq. (6). The symbol $\mathbf{G} = \mathbf{G}(\boldsymbol{k})$ is the transformation matrix detailed at Appendix 1 with $\boldsymbol{k} = (k_x, k_y)^\top$ denoting the wavevector.

Furthermore, adopting the finite element method, the governing Eq. (5) is converted to the following generalized eigenvalue problem:

$$\mathbf{K}\boldsymbol{\psi} = \omega^2\mathbf{M}\boldsymbol{\psi} \tag{8}$$

with $\boldsymbol{\psi}$ denoting the condensed eigenmode corresponding to angular frequency $\omega$. It should be pointed out that, to overcome the overestimation and underestimation of eigenfrequency caused by weak elements, element removal technique is adopted with a threshold of $10^{-3}$ for the area fraction (Xue et al., 2019; Zhang et al., 2017a). It has been verified that, on a mesh discretization of $104 \times 120$, the relative error of eigenfrequency is always below 1% as compared to the result obtained by COMSOL 5.3 with a conformal mesh.

As illustrated in Fig. 3(a,b), by solving Eq. (8), the band structure of a hexagonal UC can be obtained by sweeping the wavevector along the boundary of its irreducible first Brillouin zone $\Gamma - K - M - \Gamma$. Since the UC in Fig. 3(a) breaks the inversion and mirror symmetry, its first bandgap can be obtained by lifting the Dirac cone at $K$ point and thus non-trivial (Lu et al., 2014; Xiao et al., 2007). Following the analogy-based design method, one can combine this UC and its mirror-reflected counterpart to form a finite supercell as Fig. 3(c). Obviously, by distributing this finite strip along $x$ direction, a straight waveguide with a zig-zag interface is obtained. Therefore, the wave propagation property of the waveguide can

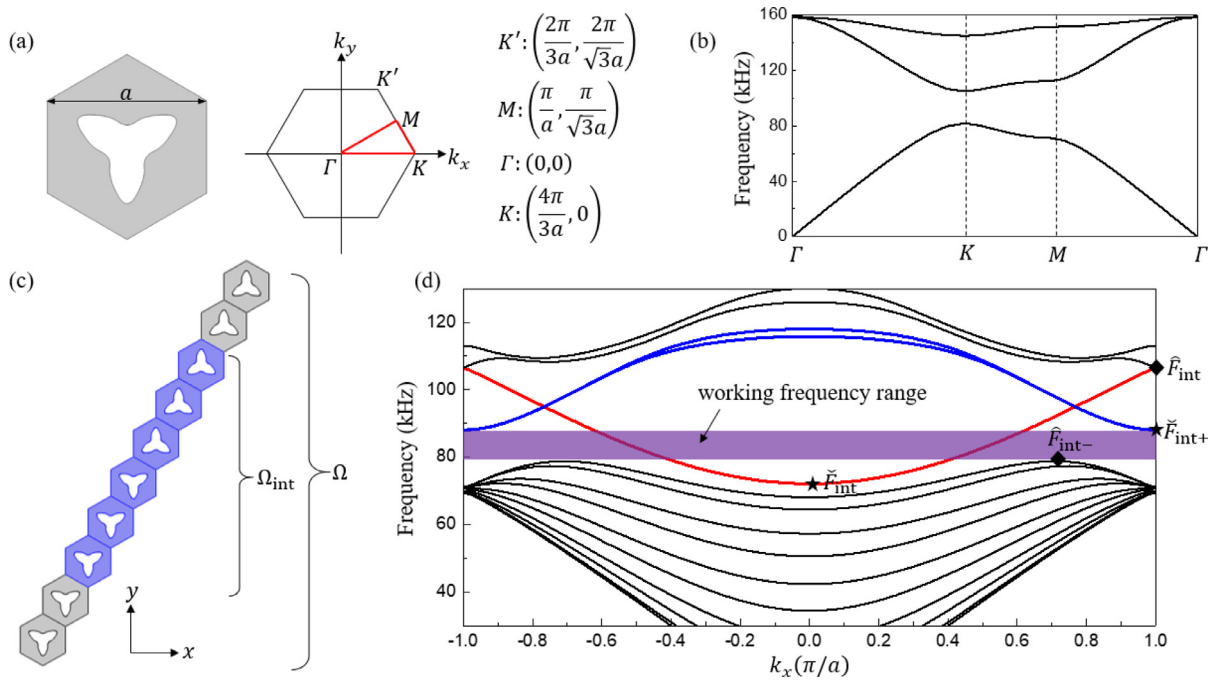


**Fig. 3.** (a) A hexagonal UC and its first irreducible Brillouin zone boundary $\Gamma - K - M - \Gamma$ (b) the band structure of the hexagonal UC (c) a finite supercell composed of the UC in (a) and its mirror reflected counterpart (d) the band structure of the supercell (black curves: bulk bands; red curve: interface band; blue curves: edge bands; purple bar: working frequency range of the interface band). (For interpretation of the references to colour in this figure legend, the reader is referred to the web version of this article.)

be determined by analyzing the finite supercell with Floquet-Bloch boundary conditions and $k_x \in [-\pi/a, \pi/a]$. In the band structure of the supercell as illustrated by Fig. 3(d), black curves are the bulk bands and the gap between the bulk bands is consistent with the first bandgap of the UC in Fig. 3(b). Inside the gap of bulk bands, an interface band (colored in red) responsible for the topological protected interfacial wave propagation and two edge bands (colored in blue) corresponding to alternative edge modes appear. Notably, a majority of the interface band is blurred by either edge bands or bulk bands, and the applicable frequency range is identified by the purple bar. This demonstrates the necessity of design valley Hall insulators through optimization method for improving the performance.

**Remark 1.** It should be noted that the design principle in the present work can also be extended to design valley Hall insulators of in-plane, three-dimensional mechanics and other physical systems by replacing the governing equations. Moreover, since the governing equation of out-of-plane problems is equivalent to the acoustic governing equation by appropriately defining the elastic constants, the optimized valley Hall insulators at out-of-plane case can be applied as optimized acoustic valley Hall insulators as well.

### 3.2. Berry curvature analysis

Berry curvature is a gauge-independent local description of the topological invariants in reciprocal space (Bernevig and Hughes, 2013; Xiao et al., 2010). Integrating the Berry curvature over the Brillouin zone gains the Berry phase or Chern number, which characterizes the topological nature of Hall insulators. Specifically, for mechanical systems, the concentrated Berry curvature near the valleys (i.e., at $K$ and $K'$ points illustrated in Fig. 3(a)) is the topological origin of the emergence of robust one-way wave transport along the interface of mechanical valley Hall insulators (Eisenberg et al., 2019; Qian et al., 2018).

Without loss of generality, in the present work, similar as the reference design (Lu et al., 2016a; 2014), the first bandgap between the first and second bands of UC is prescribed as topologically nontrival, therefore, Berry curvature is available for the first two bands. Due to the conservation law of Berry curvature (Xiao et al., 2010), i.e., $\mathcal{B}_1(k_x, k_y) = -\mathcal{B}_2(k_x, k_y)$ with $\mathcal{B}_i$ denoting the Berry curvature of $i$-th band, we only need to calculate the Berry curvature of the first band. Instead of using linear perturbation, e.g., $\boldsymbol{k}\cdot\boldsymbol{p}$ method (Voon and Willatzen, 2009), at the high-symmetry point, the Berry curvatures of the first band of evaluated designs are calculated by adopting the following formula (Chen et al., 2018a; Pal and Ruzzene, 2017):

$$\mathcal{B}_1(k_x,k_y)=2\sum_{n=2}^{N}\frac{\mathrm{Im}\left(\left(\boldsymbol{\psi}_1^{\top}\frac{\partial\mathbf{K}}{\partial k_x}\boldsymbol{\psi}_n\right)\left(\boldsymbol{\psi}_n^{\top}\frac{\partial\mathbf{K}}{\partial k_y}\boldsymbol{\psi}_1\right)\right)}{\left(\omega_1^2-\omega_n^2\right)^2} \tag{9}$$

where $N$ denotes the number of concerned eigenmodes. In present work, $N=30$ for truncation, since the denominator $(\omega_1^2-\omega_n^2)^2$ increases very quickly as $n$ getting large and and the effect of higher order eigenmodes is negligible.

According to Eq. (7), we have

$$\frac{\partial\mathbf{K}}{\partial k_x}=\frac{\partial\mathbf{G}^{\mathrm{H}}}{\partial k_x}\mathbf{K}^0\mathbf{G}+\mathbf{G}^{\mathrm{H}}\mathbf{K}^0\frac{\partial\mathbf{G}}{\partial k_x},\quad \frac{\partial\mathbf{K}}{\partial k_y}=\frac{\partial\mathbf{G}^{\mathrm{H}}}{\partial k_y}\mathbf{K}^0\mathbf{G}+\mathbf{G}^{\mathrm{H}}\mathbf{K}^0\frac{\partial\mathbf{G}}{\partial k_y} \tag{10}$$

The derivatives about transformation matrix $\mathbf{G}$ can be directly obtained according to its expression at Appendix 1.

It has been pointed out in Eisenberg et al. (2019); Qian et al. (2018), for quantum valley Hall insulators, as the non-trivial bandgap becomes larger, the topologically protected property is vanishing, which can be understood from the fading away of Berry curvature. To preserve the topological robustness of valley Hall insulators, some requirement should be proposed to preserve a confined Berry curvature. This point will be used to evaluate the topological property of the optimized designs.

## 4. Elementary inverse design methods for quantum valley Hall insulators

In this section, to construct the objective function and constraints for inverse design problems, some quantitative measures about the concerned characters of valley Hall insulators are introduced at first. Then two design strategies aiming to achieve band inverse at $K$-point in the reciprocal space and maximize the common bandgap width of a pair of valley Hall insulators are developed.

### 4.1. Quantitative measures about valley Hall insulators

#### 4.1.1. Mode inversion error

From a topological point of view, the existence of localized state is related to band inversion and quantized Chern numbers in a relevant geometric phase. Calculating the Chern number without using linear approximation, however, is computationally expensive for 2D and 3D continuum UCs. Thus we adopt the mode inversion at $K$ point to be an alternative requirement for a pair of UCs with nontrivial band structures. To apply such requirement, the mode inversion error of two UCs about their $i$-th and $(i+1)$-th bands is introduced as

$$M_{\mathrm{d}}^{[i,i+1]}=\frac{\int_{\mathrm{Y}_1\cap\mathrm{Y}_2}\left(\left|\overline{|\phi|}_{1,i}-\overline{|\phi|}_{2,i+1}\right|+\left|\overline{|\phi|}_{1,i+1}-\overline{|\phi|}_{2,i}\right|\right)d\mathrm{Y}}{\int_{\mathrm{Y}_1\cap\mathrm{Y}_2}\left(\max\left(\overline{|\phi|}_{1,i},\overline{|\phi|}_{2,i+1}\right)+\max\left(\overline{|\phi|}_{1,i+1},\overline{|\phi|}_{2,i}\right)\right)d\mathrm{Y}} \tag{11}$$

where $\mathrm{Y}_1\cap\mathrm{Y}_2$ denotes the intersection of the solid part of those two UCs, $\overline{|\phi|}_{j,i}$ is the normalized amplitude filed (i.e., with the maximum value as 1) of the $i$-th eigenmode of UC $j$ at $K$ point. Obviously, the value of $M_{\mathrm{d}}^{[i,i+1]}$ should be small when the mode inversion of the two UCs is attained.

In Eq. (11), the phase-independent amplitude field of the associated eigenmode is first normalized to be comparable. By integrating over the common solid part of the two UCs, the numerator calculates the summation of absolute differences about $i$-th mode of UC 1 with respect to $(i+1)$-th mode of UC 2 and $(i+1)$-th mode of UC 1 with respect to $i$-th mode of UC 2. In the denominator, pointwise maximized amplitude fields are integrated. In this manner, the mode inversion error is always between 0 and 1, and perfect mode inversion achieves at $M_{\mathrm{d}}^{[i,i+1]}=0$. We will show that this measure can either be used as objective function or a constraint to effectively achieve the mode inversion.

#### 4.1.2. Common bandgap width

Since the interface mode generally appears in the nontrivial common bandgap of a pair of TIs, some works adopt the common bandgap width as an indicator for the width of working frequency range (i.e., operating bandwidth) of TIs (Chen et al., 2019b). The common bandgap width of a pair of UCs at $i$-th and $(i+1)$-th bands can be expressed as:

$$F_{\mathrm{com}}^{[i,i+1]}=\min\left(\left(\check{F}_{1,i+1}-\hat{F}_{1,i}\right),\left(\check{F}_{2,i+1}-\hat{F}_{2,i}\right),\left(\check{F}_{1,i+1}-\hat{F}_{2,i}\right),\left(\check{F}_{2,i+1}-\hat{F}_{1,i}\right)\right) \tag{12}$$

where $\hat{F}_{1,i}$ is the maximum frequency at $i$-th band of UC 1 while $\check{F}_{2,i+1}$ is the minimum frequency at $(i+1)$-th band of UC 2, respectively. However, as shown later, gap may appear between the interface band and bulk bands of the supercell when the common bandgap is extra wide.

### 4.2. Elementary inverse design strategies

#### 4.2.1. Inverse design of valley Hall insulators by achieving band inversion

Different as traditional design method through manually breaking the symmetry of UCs with Dirac cone feature, we suggest to directly search a pair of topologial insulators among the admissible UC-set to minimize the corresponding mode

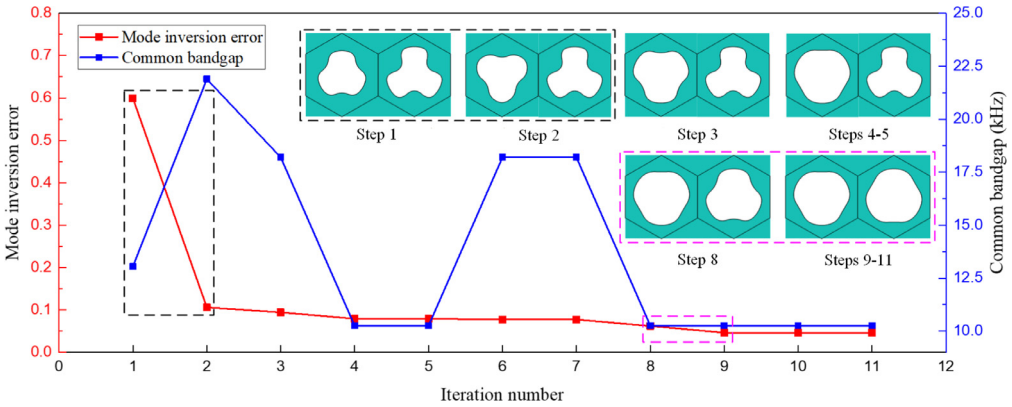


**Fig. 4.** Iteration history of inverse design topology insulators by minimizing mode inversion error at *K*-point with a common bandgap width constraint.

**Table 1**
The first two eigenmodes and Poynting vectors of the intermediate designs at *K*-point .

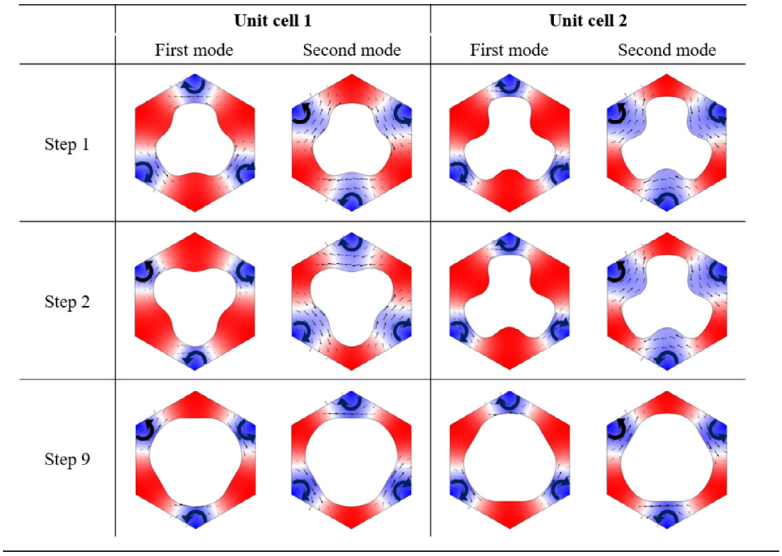


inversion error through solving the following optimization formulation:

$$\begin{aligned} &\min_{\boldsymbol{D}\subset\mathcal{U}_{\boldsymbol{D}}} && M_{\mathrm{d}}^{[1,2]}(\boldsymbol{D}) \\ &\text{s.t.} && F_{\mathrm{com}}^{[1,2]} \geq \overline{F} \end{aligned} \tag{13}$$

where $\boldsymbol{D} = ((\boldsymbol{D}^1)^\top, (\boldsymbol{D}^2)^\top)^\top$ is the design variable vector describing the voids for two UCs and $\mathcal{U}_{\boldsymbol{D}}$ is the corresponding admissible set. The left-hand-side of the constraint is actually the common bandgap width between the first two bands of the two UCs, and the right-hand-side $\overline{F}$ is a desired value of the common bandgap width.

For simplicity, we adopt 12 control points for the central void and assume the UCs are $C_{3v}$ symmetric as Fig. 2(c). By setting $\overline{F} = 10.0\text{kHz}$ and $\mathcal{U}_{\boldsymbol{D}} = \{(r_1^1, r_2^1, r_3^1, r_1^2, r_2^2, r_3^2)^\top | 0.2\text{cm} \leq r_j^i \leq 0.7\text{cm}, i = 1, 2; j = 1, 2, 3\}$, formulation (13) is solved using GA in Matlab 2016b with default setting except for 60 individuals per generation (Chipperfield and Fleming, 1995). The iteration history of the UCs recording the mode inversion error at *K*-point and the width of common bandgap between the first two bands are presented in Fig. 4. It can be found that, within 10 generations, the optimized result $\boldsymbol{D}^{\text{opt}} = (0.6, 0.7, 0.7, 0.7, 0.7, 0.6)^\top\text{cm}$ is obtained. During the optimization, the mode difference error gradually decreases from about 0.6 and finally converges to a small value 0.05, while the width of common bandgap finally converges to 10.2kHz, which is greater than $\overline{F}$. It should be noted that, from step 1 to step 2, there is a sharp decline in the mode inversion error, and the void in left UC is flipped to become opposite as that in the right UC. From step 8 to step 9, the right UC is evolved to be the mirror-reflected counterpart of left UC and this further decreases the mode difference error. The mode shapes and the Poynting vectors of the UCs at steps 1, 2, 9 are presented in Table 1, which explains the sharp decline during iterations

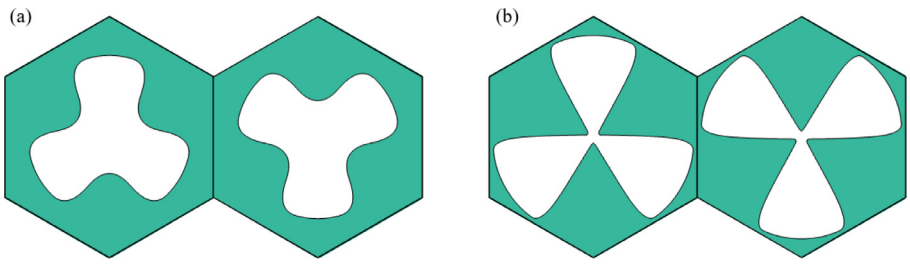


**Fig. 5.** Optimized $C_{3v}$-symmetric insulators by maximizing the common bandgap width with a mode inversion error constraint (a) 12 control point case (b) 24 control point case.

and the optimality of the final design. This example demonstrates the effectiveness of the proposed mode inversion error on controlling the band inversion of a pair of valley Hall insulators.

*4.2.2. Inverse design of valley Hall insulators by maximizing the common bandgap width*

Here we consider the following formulation to maximize the common bandgap width of two UCs while preserving the mode inversion at *K*-point:

$$\begin{aligned} &\max_{\boldsymbol{D}\subset\mathcal{U}_{\boldsymbol{D}}} \quad F^{[1,2]}(\boldsymbol{D}) \\ &\text{s.t.} \qquad\quad M_{\mathrm{d}}^{[1,2]}(\boldsymbol{D}) \le \overline{M}_{\mathrm{d}} \end{aligned} \tag{14}$$

with $\overline{M}_{\mathrm{d}}$ denoting a tolerance for the mode inversion error. By using 12 control points for the $C_{3v}$-symmetric central void, and setting $\overline{M}_{\mathrm{d}} = 0.30$ and $\mathcal{U}_{\boldsymbol{D}} = \{(r_1^1, r_2^1, r_3^1, r_1^2, r_2^2, r_3^2) | 0.2\mathrm{cm} \le r_j^i \le 0.7\mathrm{cm}, i = 1, 2;\ j = 1, 2, 3\}$, the optimized insulators described by $\boldsymbol{D}^{\mathrm{opt}} = (0.2, 0.7, 0.7, 0.7, 0.7, 0.2)^\top\mathrm{cm}$ is obtained with a common bandgap width of 32.7kHz as illustrated in Fig. 5(a). To further enlarge the design space, 24 control points is adopted with 10 design variables as illustrated in Fig. 2(d) to describe the central void. By searching within $\mathcal{U}_{\boldsymbol{D}} = \{(r_1^1, \ldots, r_5^1, r_1^2, \ldots, r_5^2)^\top | 0.05\mathrm{cm} \le r_j^i \le 0.85\mathrm{cm}, i = 1, 2;\ j = 1, \ldots, 5\}$, the optimized solution is $\boldsymbol{D}^{\mathrm{opt}} = (0.05, 0.05, 0.84, 0.85, 0.85, 0.85, 0.85, 0.84, 0.05, 0.05)^\top\mathrm{cm}$ with a common bandgap width of 67.8kHz. The corresponding optimized insulators are illustrated in Fig. 5(b). Notice that in the present work, focusing on verifying the effectiveness of minimizing the band inversion error and maximizing the common bandgap width, most of the bounds are reached in the above optimized designs and this implies that the achievable performance is restricted by those geometrical constraints. We would like to further address this point in future work by incorporating more voids and more relaxed bounds.

*4.2.3. Evaluation of the optimized insulators*

By noticing the same tendency applies for all wavevectors, in Table 2, the 5th to 15th bands and the interface modes at $k_x = 0$ and $k_x = \pi/(2a)$ of the optimized valley Hall insulators are presented for illustration. For the design with a common bandgap width of 10.2kHz, the interface band has common frequency ranges with bulk bands. As the width of common bandgap increases to 32.7kHz, the interface band is separated from the bulk bands. By further increasing the common bandgap width to 67.8kHz, both the interface band and the bulk bands become flatter and gap appears between them. Furthermore, by comparison, it can be found as the common bandgap width increases, the interface modes become more concentrated around the interface. It is also worth noting that, Stainko and Sigmund achieved to systematically design photonic waveguides in terms of maximizing the interface confinement and tailoring the dispersion properties by topology optimization method (Stainko and Sigmund, 2007).

On the other hand, to evaluate the topological property of the obtained designs, the Berry curvatures of the first band of the optimized designs are calculated according to Eq. (9). As shown in Fig. 6(a–c), while the width of common bandgap is increased from 10.2kHz to 67.8kHz, the peak value of Berry curvature decreases dramatically and the Berry curvature is unconfined in the reciprocal space. Actually, this observation is quite consistent with the assertion made in (Eisenberg et al., 2019; Qian et al., 2018): as the bandgap becomes larger, the topological protected property is vanishing, which can be understood from the fading away of Berry curvature.

The results in Table 2 and Fig. 6(a–c) imply that, the common bandgap width cannot accurately measure the operating bandwidth since either intersection or gap may exist between the interface band and bulk bands; in addition, by maximizing the width of common bandgap, the interface mode gets more concentrated, while the topological robustness is sacrificed. Those contradictions lead to the concept of "optimal valley Hall insulators" in the forthcoming section.

## 5. Optimal quantum valley Hall insulators

In this section, an exact measure about the relative operating bandwidth of valley Hall insulators are at first introduced, then the design concept of "optimal quantum valley Hall insulators" is realized by solving an optimization formulation, and the corresponding optimized designs are verified finally.

**Table 2**
The 5th to 15th bands and two illustrative interface modes of the optimized designs with red curves denoting the interface bands .

| Common bandgap | Band structure of finite supercell | Interface modes $k_x = 0$ | Interface modes $k_x = \pi/(2a)$ |
|---|---|---|---|
| 10.2kHz | 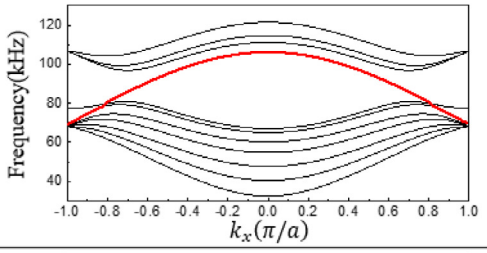 | 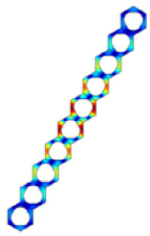 | 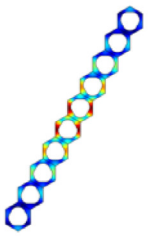 |
| 32.7kHz | 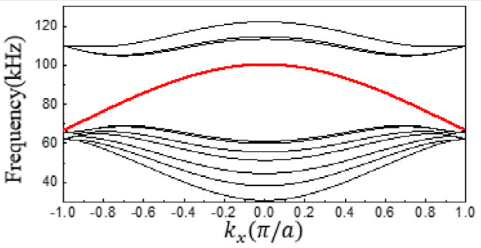 | 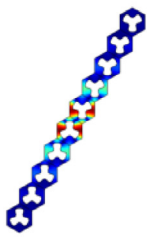 | 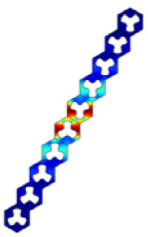 |
| 67.8kHz | 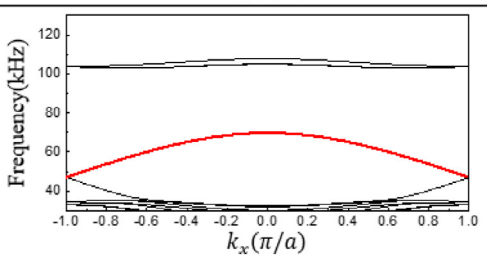 | 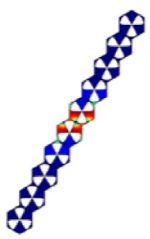 | 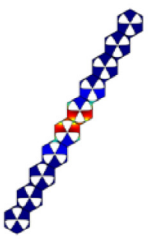 |

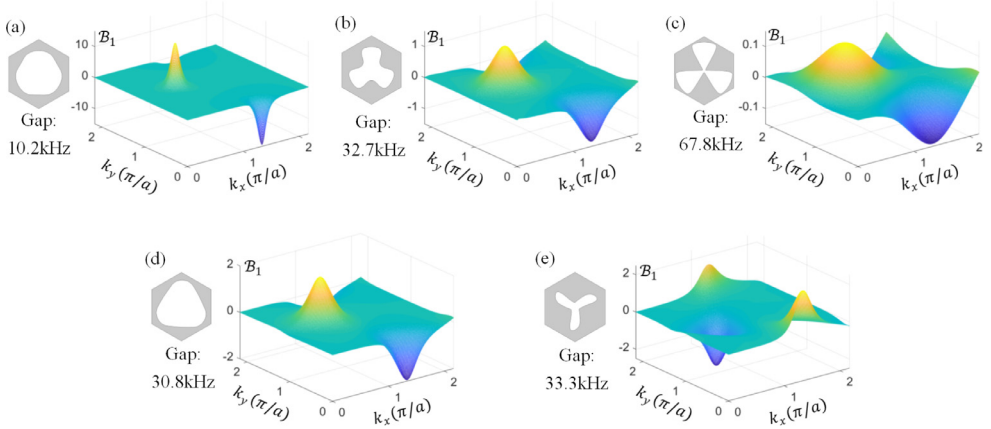


**Fig. 6.** Berry curvatures in reciprocal space $\left[0, \frac{5\sqrt{3}\pi}{4a}\right] \times \left[0, \frac{5\sqrt{3}\pi}{4a}\right]$ of (a) UC 1 of valley Hall insulators obtained by minimizing mode inversion error (b) UC 1 of valley Hall insulators by maximizing the common bandgap width with 12 control points (c) UC 1 of valley Hall insulators by maximizing common bandgap width with 24 control points (d) UC 1 of the optimized valley Hall insulators (e) UC 2 of the optimized valley Hall insulators.

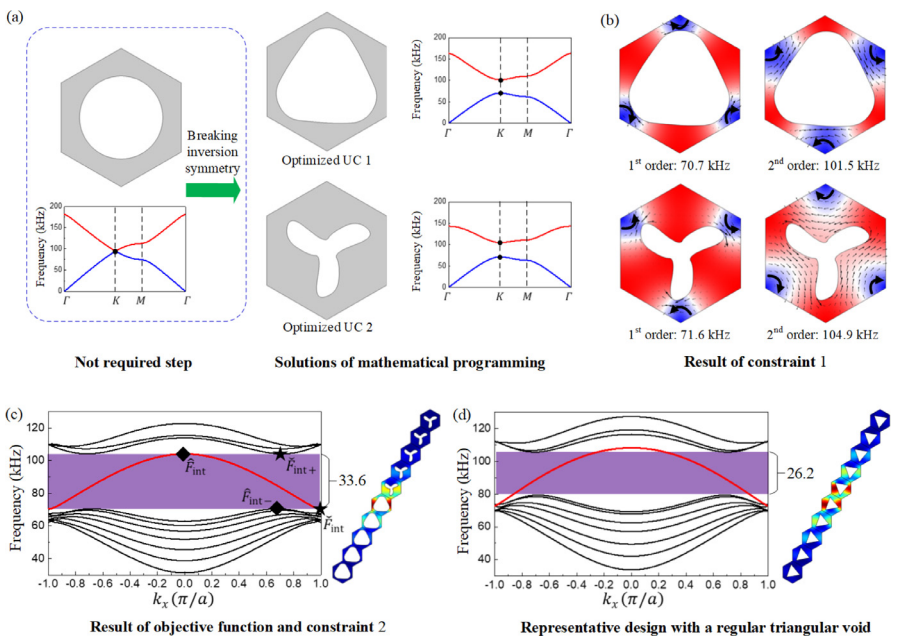


**Fig. 7.** (a) Optimized valley Hall insulators obtained by the proposed inverse design method (b) mode inversion at *K*-point between the first two bands (c) the band structure and interface mode at $k_x = 0.5\pi/a$ of the optimized finite supercell (d) the band structure and interface mode at $k_x = 0.5\pi/a$ of the reference finite supercell. (For interpretation of the references to colour in this figure legend, the reader is referred to the web version of this article.)

### 5.1. Exact measure about relative operating bandwidth

#### 5.1.1. Interface mode intensity and identification of the interface band

For a finite supercell with an interface band, the interface mode intensity is introduced to measure the concentration of the corresponding interface mode as

$$I = \frac{\int_{\Omega_{\text{int}}} |\phi| d\Omega}{\int_{\Omega} |\phi| d\Omega} \tag{15}$$

with $\Omega_{\text{int}}$ and $\Omega$ denoting the interface region and the whole supercell as illustrated in Fig. 3(a). During implementation, it is found that distributing 5 UCs on each side of interface and selecting the central 6 UCs as the interface region works well for Eq. (15).

With this formula in mind, the average interface mode intensity of a band can be easily calculated. The interface band can be identified automatically by comparing the average intensity of each band.

#### 5.1.2. Operating bandwidth of an interface band

With the interface band identified (i.e., the red band in Fig. 3(b)), one can easily find its upper adjacent band and lower adjacent band, respectively. Then the operating bandwidth of the interface band can be calculated as

$$W = \min\left(\hat{F}_{\text{int}}, \check{F}_{\text{int}+}\right) - \max\left(\check{F}_{\text{int}}, \hat{F}_{\text{int}-}\right) \tag{16}$$

where $\hat{F}_{\text{int}}, \check{F}_{\text{int}}$ are the maximum and minimum frequency values of the interface band. The symbols $\check{F}_{\text{int}+}$ and $\hat{F}_{\text{int}-}$ are the minimum frequency of the upper adjacent band and maximum value of the lower adjacent band of the interface band, respectively; see Fig. 3(d) for reference.

#### 5.1.3. Relative operating bandwidth of the interface band

It should be noted that, in general, maximizing the bandwidth would probably push the bands to higher frequencies. A more meaningful choice is to consider the relative operating bandwidth of the interface band as

$$\overline{W} = \frac{2\left(\min\left(\hat{F}_{\text{int}}, \check{F}_{\text{int}+}\right) - \max\left(\check{F}_{\text{int}}, \hat{F}_{\text{int}-}\right)\right)}{\min\left(\hat{F}_{\text{int}}, \check{F}_{\text{int}+}\right) + \max\left(\check{F}_{\text{int}}, \hat{F}_{\text{int}-}\right)} \tag{17}$$

This measure will be used for optimal design of valley Hall insulators in the following.

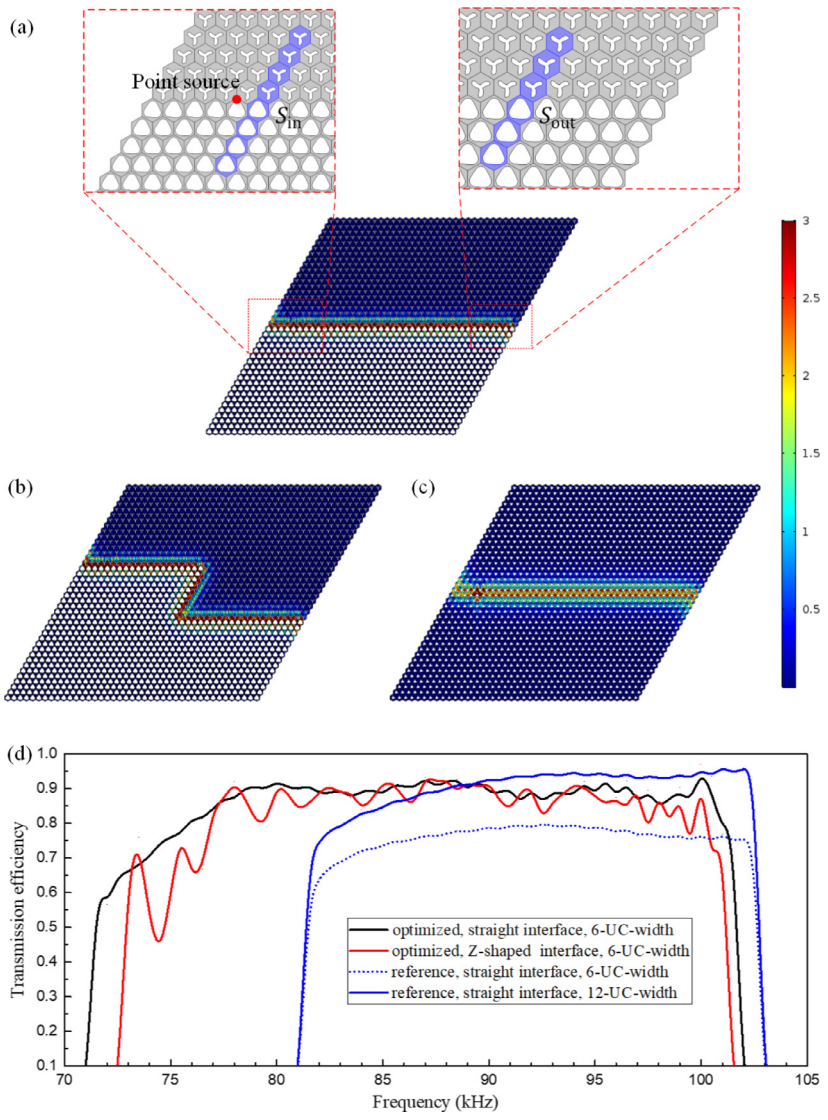


**Fig. 8.** Topologically protected elastic wave propagation at frequency of 90kHz (a) along a straight interface of optimized valley Hall insulators (b) along a *Z*-shaped interface of optimized valley Hall insulators (c) along a straight interface of reference insulators; (d) transmission efficiency spectra of considered waveguides: black curve ($S_{\text{out}}$ contains 6-UC-width of optimized design); red curve ($S_{\text{out}}$ contains 6-UC-width of optimized design); blue dotted curve ($S_{\text{out}}$ contains 6-UC-width of reference design); black solid curve ($S_{\text{out}}$ contains 12-UC-width of reference design). (For interpretation of the references to colour in this figure legend, the reader is referred to the web version of this article.)

### 5.2. Optimal valley Hall insulators

Taking into consideration of large relative operating bandwidths, highly confined interface modes and topological robustness, we propose the concept of "optimal valley Hall insulators" as: the corresponding supercell possessing a gapless band structure and an interface band with the largest relative operating bandwidth, which can be formulated into the following optimization formulation:

$$\begin{aligned} &\max_{\boldsymbol{D}\subset\mathcal{U}_{\boldsymbol{D}}} && \overline{W}(\boldsymbol{D}) \\ &\text{s.t.} && M_{\text{d}}^{[1,2]}(\boldsymbol{D}) \le \overline{M}_{\text{d}} \\ & && |\hat{F}_{\text{int}} - \check{F}_{\text{int}+}| + |\check{F}_{\text{int}} - \hat{F}_{\text{int}-}| \le \overline{F} \end{aligned} \tag{18}$$

During solving this optimization problem, the central void is assumed to be $C_3$-symmetric and described by 12 controls point as illustrated by Fig. 2(a,b) with $\mathcal{U}_{\boldsymbol{D}} = \{(r_1^1, r_2^1, r_3^1, r_4^1, \theta^1, r_1^2, r_2^2, r_3^2, r_4^2, \theta^2)^\top | 0.1\text{cm} \le r_j^i \le 0.8\text{cm}, 0 \le \theta^i \le 30^\circ, i = 1, 2; j = 1, \ldots, 4\}$. The first constraint with $\overline{M}_{\text{d}} = 0.20$ is used to preserve the band inversion at *K*-point between the first two bands of the UCs and the existence of interface band for the corresponding supercell. The second constraint is to make sure there

neither exists gap nor intersection between the interface band and the adjacent bands, which is used to guarantee the quantum valley Hall effect of optimized designs. This optimization formulation is also solved by GA and more details about the solution process are available in Appendix 2.

The optimized valley Hall insulators are plotted in Fig. 7(a), corresponding to $\boldsymbol{D}^{\text{opt}} = (0.61\text{cm}, 0.62\text{cm}, 0.80\text{cm}, 0.80\text{cm}, 12.5^\circ, 0.75\text{cm}, 0.63\text{cm}, 0.27\text{cm}, 0.10\text{cm}, 15^\circ)^\top$. With a mode inversion error of 0.14 satisfying the constraint 1 in optimization formulation (18), the mode inversion is achieved at $K$-point between the first two bands, as verified by the mode shapes and the corresponding Poynting vectors in Fig. 7(b). From another point of view, as illustrated by Fig. 7(a), UC 1 and UC 2 can be obtained by breaking the inversion symmetry of the hexagon with a central circular to induce topologically nontrivial bandgaps. Notably, such process is not required in the proposed inverse design method and optimized insulators are directly characterized with the help of constraint 1. Besides, the geometry of the pair of optimized valley Hall insulators is quite different, and this enjoys more design freedom and is difficult to be obtained by intuition.

In the band structure of the optimized finite supercell, $\hat{F}_{\text{int}} = \check{F}_{\text{int}+} = 104.1\text{kHz}$, $\check{F}_{\text{int}} = 70.4\text{kHz}$, $\hat{F}_{\text{int}-} = 70.5\text{kHz}$, which corresponds to an optimized relative operating bandwidth of 38.5%. As a reference, illustrated by Fig. 7(d) and Lu et al. (2014), the reference valley Hall insulators containing regular triangular voids with filling ratio of 0.24 and rotations of $\alpha = \pm 20^\circ$ are evaluated. The relative operating bandwidth of the reference designs is 28.4%. In addition, the interface modes of those supercells at $k_x = 0.5\pi/a$ in Fig. 7 (c,d) show a better concentration near the interface of the optimized insulators. This implies that, for the optimized supercell, the relative operating bandwidth is maximized, while there is almost no gap between the interface band and bulk bands, due to the effects of objective function and constraint 2.

In addition, as pointed out by Eisenberg et al. (2019); Qian et al. (2018), a confined Berry curvature is necessary for a robust valley Chern effect. The Berry curvatures of our optimized insulators are presented in Fig. 6(d,e). As compared to the Berry curvatures of optimized designs by purely maximizing the common bandgap width illustrated by Fig. 6(b,c), a well-confined distribution of Berry curvature is achieved with the help of the gapless constraint (i.e., constraint 2) and this guarantees the topological robustness of the optimized valley Hall insulators. Therefore, the idea of "a gapless band structure" presents an effective requirement for engineering the Berry curvature to preserve the topological property of quantum valley Hall effect.

In summary, the proposed design concept and the corresponding optimization formulation, i,e., to find a pair of insulators with band inversion while the corresponding finite supercell has a gapless band structure with the relative operating bandwidth maximized, present an effective way to design optimized valley Hall insulators through rationally engineering band structure and Berry curvature.

### 5.3. Verification and comparison

To further evaluate the optimized valley Hall insulators, as the experiments in Yan et al. (2018), waveguides containing a straight interface and a $Z$-shaped interface composed of $41 \times 40$ optimized UCs are modelled in COMSOL with absorbing boundary conditions. As illustrated in Fig. 8(a), an unit monopole point source is applied at the point with a $4a$ distance from the left side of interface. Transmission efficiency is calculated according to the expression $\int_{S_{\text{out}}} |u| dS \Big/ \int_{S_{\text{in}}} |u| dS$. As comparison, the waveguide composed by the reference insulators containing a straight interface is also analyzed. Obviously, elastic wave can robustly pass all the interfaces even containing sharp corners with no backscattering, and the propagation is more concentrated in the interface of optimized waveguide. Besides, with the same monopole point source, the displacement amplitude near the optimized interface is larger and the localization around the source location is alleviated in the optimized design, which may also be an interesting phenomena for real applications.

The transmission efficiency spectra is shown in Fig. 8(d) for the frequency ranges corresponding to interfacial transport for clarity. It can be summarized that: (1) the frequency ranges corresponding to interfacial transport are quite consistent with the working frequency ranges of the interface bands predicted by Fig. 7(c,d) and this demonstrates the rationality of objective function in optimization formulation (18); (2) the transmission efficiency along a straight interface and along a $Z$-shaped interface is both close to 1, which verifies the robustness of the interfacial transport of the optimized waveguide; (3) the topologically protected interfacial transport of the optimized waveguide has a wider working frequency range and can be well-concentrated in a 6-UC-width region.

To demonstrate the one-way propagation more clearly, as illustrated in Fig. 9(a), at the center of the optimized $Z$-shaped waveguide, eight monopole sources equally distributing along the circumference of a circular with a small radius (i.e., $a/(10\sqrt{3})$) are simultaneously applied through the following manner: $u_k = \exp(\pm \text{i} k\pi/4), k = 1, 2, \ldots, 8$ with i denoting the imaginary number. At 90kHz, for the case $u_k = \exp(-\text{i} k\pi/4), k = 1, 2, \ldots, 8$, only the positive group velocity is stimulated. Fig. 9(a) illustrates that the elastic wave only propagates forward and passes through the lower sharp corner without any backscattering. This fact can be further observed from the energy flow vectors near the $Z$-shaped interface region presented in Fig. 9(b). On the opposite, applying the source $u_k = \exp(\text{i} k\pi/4), k = 1, 2, \ldots, 8$, only backward propagation is stimulated and the corresponding one-way propagated displacement magnitude filed and the energy flow vectors are illustrated in Fig. 9(c,d), respectively.

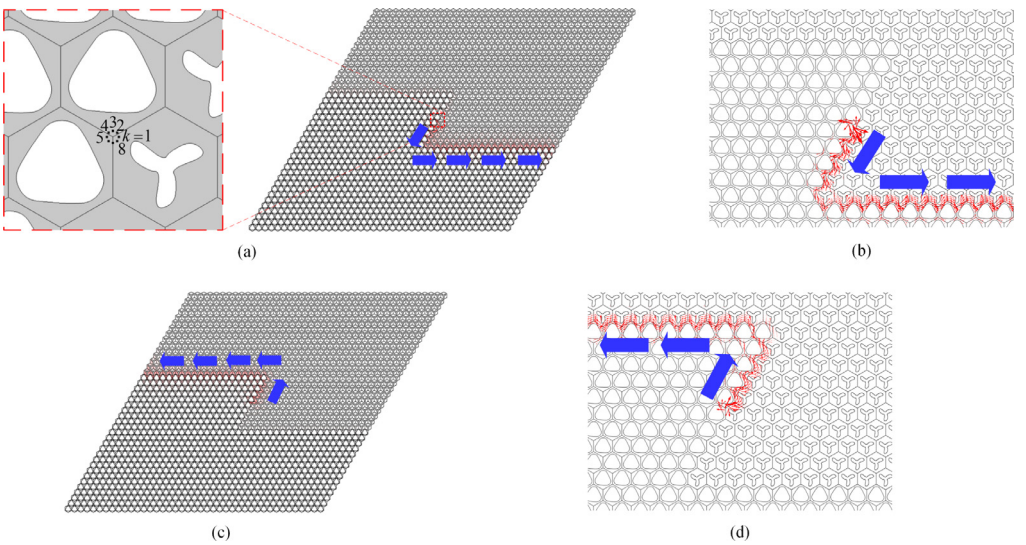


**Fig. 9.** (a) Imposing excitation with different phases through 8 monopole sources (enlarged window) and displacement magnitude field at steady state with respect to stimulation $u_k = \exp(-\mathrm{i}k\pi/4)$ (b) energy flow vectors near the *Z*-shaped interface region with respect to stimulation $u_k = \exp(-\mathrm{i}k\pi/4)$ (c) displacement magnitude field with respect to stimulation $u_k = \exp(\mathrm{i}k\pi/4)$; energy flow vectors with respect to stimulation $u_k = \exp(\mathrm{i}k\pi/4)$.

## 6. Conclusion remarks

With the introduction of quantitative measures about the relative operating bandwidth and the mode inversion error, a new inverse design paradigm of "optimal valley Hall insulators" is presented. Different from analogy-based trial-and-error design approach, optimized valley Hall insulators can be systematically obtained by solving an optimization formulation with help of the modified MMV method. Through rationally engineering the band structure and Berry curvature, the optimized design preserves a simple geometry and significantly outperforms a reference design in literature in terms of relative operating bandwidth and field intensity. Such strategy can be easily extended to systematically design other topological insulators, such as spin-Hall insulators and higher-order topological insulators in different physical systems. In addition, the efficiency of explicit structural optimization method in describing continuum unit cells (Guo et al., 2019) and optimization aided inverse band structure and Berry curvature engineering can be more significant for complex systems, e.g., multi-materials, three dimensional cases and optimal control problems (Grigorenko and Rabitz, 2009), while intuitive tuning is inefficient or even infeasible.

## Declaration of Competing Interest

There are no conflicts to declare.

## Acknowledgements

This work is supported by the Air Force Office of Scientific Researchunder grant no. AF 9550-18-1-0342 with Program Manager Dr. Byung-Lip (Les) Lee, the NSF EFRI under Grant No. 1641078 and the Army Research Office under grant no. W911NF-18-1-0031 with Program Manager Dr. David M. Stepp. In addition, the authors would like to thank Prof. Emil Prodan for valuable discussions regarding Berry curvature of valley Hall insulators.

## Appendix A. Finite element implementation of Floquet-Bloch boundary conditions on a fixed Cartesian mesh

As illustrated in Fig. 10(a), the nodes are classified into 13 groups, i.e., Left-top Boundary nodes (LtB), Left Boundary nodes (LB), Left-bottom Boundary nodes (LbB), Right-bottom Boundary nodes (RbB), Right Boundary nodes (RB), Right-top Boundary nodes (RtB), Top Corner nodes (TC), Left-top Corner node (LtC), Left-bottom Corner node (LbC), Bottom Corner node (BC), Right-bottom Corner node (RbC), Right-top Corner node (RtC) and Rest Free nodes (RF). The Floquet-Bloch boundary

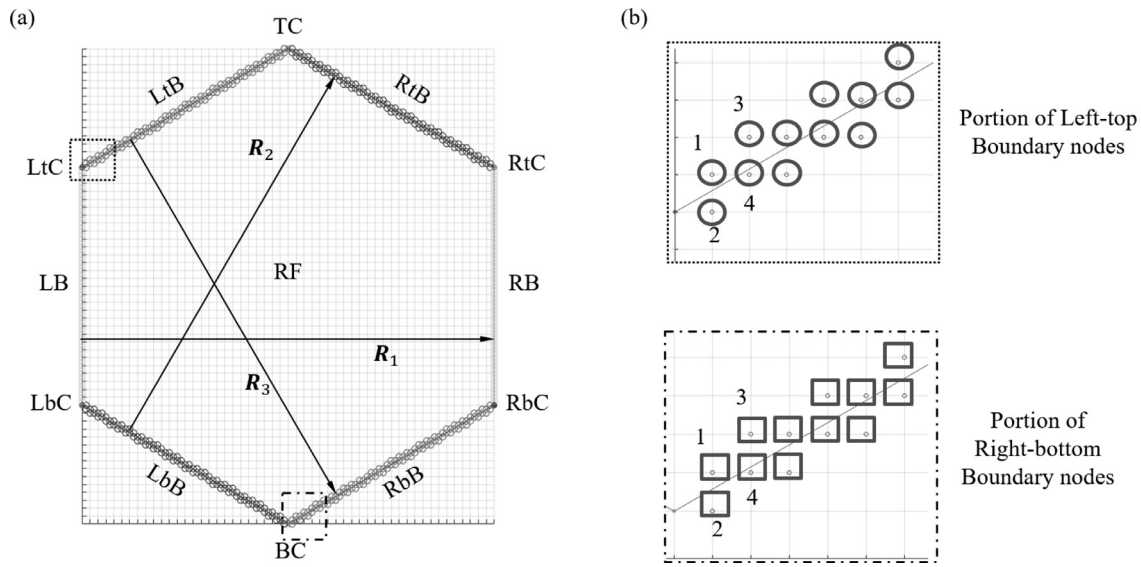


**Fig. 10.** Implementation of Floquet-Bloch boundary conditions for a hexagonal UC with a fixed Cartesian mesh (a) classification of nodes (b) enlarged drawing of framed boundary nodes in (a).

condition can be expressed as following:

$$\begin{pmatrix} u_{\mathrm{LtC}} \\ u_{\mathrm{LbC}} \\ u_{\mathrm{RtC}} \\ u_{\mathrm{RbC}} \\ u_{\mathrm{TC}} \\ u_{\mathrm{BC}} \\ u_{\mathrm{LtB}} \\ u_{\mathrm{LB}} \\ u_{\mathrm{LbB}} \\ u_{\mathrm{RbB}} \\ u_{\mathrm{RB}} \\ u_{\mathrm{RtB}} \\ u_{\mathrm{RF}} \end{pmatrix} \triangleq \boldsymbol{U}_{\mathrm{tot}} = \begin{bmatrix} \mathbf{I} & \mathbf{0} & \mathbf{0} & \mathbf{0} & \mathbf{0} & \mathbf{0} \\ \mathbf{0} & \mathbf{I} & \mathbf{0} & \mathbf{0} & \mathbf{0} & \mathbf{0} \\ e^{i\boldsymbol{k}\cdot\boldsymbol{R}_1}\mathbf{I} & \mathbf{0} & \mathbf{0} & \mathbf{0} & \mathbf{0} & \mathbf{0} \\ \mathbf{0} & e^{i\boldsymbol{k}\cdot\boldsymbol{R}_1}\mathbf{I} & \mathbf{0} & \mathbf{0} & \mathbf{0} & \mathbf{0} \\ \mathbf{0} & e^{i\boldsymbol{k}\cdot\boldsymbol{R}_2}\mathbf{I} & \mathbf{0} & \mathbf{0} & \mathbf{0} & \mathbf{0} \\ e^{i\boldsymbol{k}\cdot\boldsymbol{R}_3}\mathbf{I} & \mathbf{0} & \mathbf{0} & \mathbf{0} & \mathbf{0} & \mathbf{0} \\ \mathbf{0} & \mathbf{0} & \mathbf{I} & \mathbf{0} & \mathbf{0} & \mathbf{0} \\ \mathbf{0} & \mathbf{0} & \mathbf{0} & \mathbf{I} & \mathbf{0} & \mathbf{0} \\ \mathbf{0} & \mathbf{0} & \mathbf{0} & \mathbf{0} & \mathbf{I} & \mathbf{0} \\ \mathbf{0} & \mathbf{0} & e^{i\boldsymbol{k}\cdot\boldsymbol{R}_3}\mathbf{I} & \mathbf{0} & \mathbf{0} & \mathbf{0} \\ \mathbf{0} & \mathbf{0} & \mathbf{0} & e^{i\boldsymbol{k}\cdot\boldsymbol{R}_1}\mathbf{I} & \mathbf{0} & \mathbf{0} \\ \mathbf{0} & \mathbf{0} & \mathbf{0} & \mathbf{0} & e^{i\boldsymbol{k}\cdot\boldsymbol{R}_2}\mathbf{I} & \mathbf{0} \\ \mathbf{0} & \mathbf{0} & \mathbf{0} & \mathbf{0} & \mathbf{0} & \mathbf{I} \end{bmatrix} \begin{pmatrix} u_{\mathrm{LtC}} \\ u_{\mathrm{LbC}} \\ u_{\mathrm{LtB}} \\ u_{\mathrm{LB}} \\ u_{\mathrm{LbB}} \\ u_{\mathrm{RF}} \end{pmatrix} \triangleq \mathbf{G}((\boldsymbol{k}))\boldsymbol{U} \tag{19}$$

where $\boldsymbol{k}$ denotes the wavevector, $\boldsymbol{U}_{\mathrm{tot}}$ and $\boldsymbol{U}$ are the displacement vectors with full degree-of-freedom and condensed degree-of-freedom, respectively. The symbol $\mathbf{G}(\boldsymbol{k})$ is the transformation matrix between the full displacement vector and the condensed counterpart.

## Appendix B. Solution process of the inverse design for optimal valley Hall insulators

During the solution process of the optimization formulation for inverse design of optimal valley Hall insulators, to accelerate the convergence, penalty function method is adopted to combine the objective function and constraint 2 of optimization formulation (18) as:

$$f = -W^{[1,2]}(\boldsymbol{D}) + p(F_{\mathrm{gp}}(\boldsymbol{D}))F_{\mathrm{gp}}(\boldsymbol{D}) \tag{20}$$

with $F_{\mathrm{gp}} = |\hat{F}_{\mathrm{int}} - \check{F}_{\mathrm{int}+}| + |\check{F}_{\mathrm{int}} - \hat{F}_{\mathrm{int}-}|$ and $p$ is the penalty function defined as:

$$p(F_{\mathrm{gp}}) = \begin{cases} 1, & \text{if } F_{\mathrm{gp}} \le 0.5\mathrm{kHz} \\ 3, & \text{if } 0.5\mathrm{kHz} < \mathrm{F_{gp}} \le 1\mathrm{kHz} \\ 5, & \text{otherwise} \end{cases}$$

By minimizing the modified objective function Eq. (20) together with constraint 1 in optimization formulation (18) for mode inversion requirement, a pair of valley Hall insulators with maximized relative operating bandwidth and minimized gap/intersection between the interface band and its adjacent bands can be obtained. To further save computational effort, as the flow chart illustrated by Fig. 11, in the evaluation module, the more expensive finite supercell analysis is only implemented for individuals achieved mode inversion.

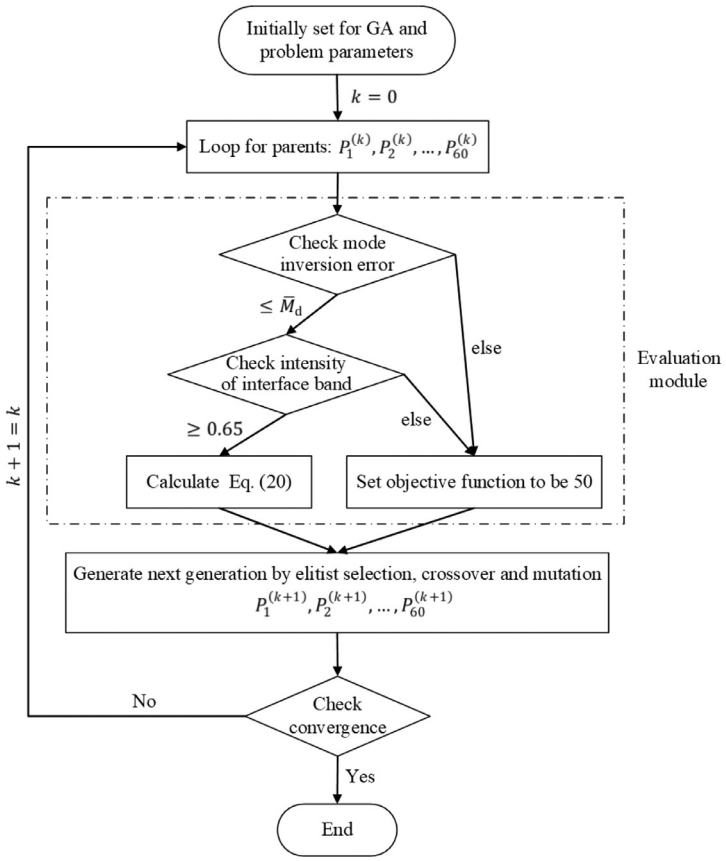


**Fig. 11.** Flowchart of the inverse design procedure of optimized valley Hall insulators.

## References


Achenbach, J., 2012. Wave Propagation in Elastic Solids. Elsevier.
Bendsøe, M.P., Sigmund, O., 2004. Topology Optimization: Theory, methods, and applications. Springer.
Bernevig, B.A., Hughes, T.L., 2013. Topological Insulators and Topological Superconductors. Princeton University Press.
Berry, M.V., 1984. Quantal phase factors accompanying adiabatic changes. Proceed. Roy. Soc. Lond. A Math. Phys. Sci. 392 (1802), 45–57.
Chen, H., Nassar, H., Huang, G., 2018. A study of topological effects in 1D and 2D mechanical lattices. J. Mech. Phys. Solid. 117, 22–36.
Chen, H., Nassar, H., Norris, A.N., Hu, G., Huang, G., 2018. Elastic quantum spin Hall effect in kagome lattices. Phys. Rev. B 98 (9), 94302.
Chen, H., Yao, L., Nassar, H., Huang, G., 2019. Mechanical quantum Hall effect in time-modulated elastic materials. Phys. Rev. Appl. 11 (4), 44029.
Chen, Y., Meng, F., Jia, B., Li, G., Huang, X., 2019. Inverse design of photonic topological insulators with extra-wide bandgaps. Phys. Status Solid. (RRL)–Rap. Res. Lett. 1900175.
Chipperfield, A., Fleming, P., 1995. The MATLAB Genetic Algorithm Toolbox. IET.
Christiansen, R.E., Wang, F., Sigmund, O., 2019. Topological insulators by topology optimization. Phys. Rev. Lett. 122 (23), 234502.
Christiansen, R.E., Wang, F., Sigmund, O., Stobbe, S., 2019. Designing photonic topological insulators with quantum-spin-Hall edge states using topology optimization. Nanophotonics 8 (8), 1363–1369.
Dong, J.W., Chen, X.D., Zhu, H., Wang, Y., Zhang, X., 2017. Valley photonic crystals for control of spin and topology. Nat. Mater. 16 (3), 298.
Eisenberg, Y., Barlas, Y., Prodan, E., 2019. Valley Chern effect with LC resonators: a modular platform. Phys. Rev. Appl. 11 (4), 44077.
Gao, F., Xue, H., Yang, Z., Lai, K., Yu, Y., Lin, X., Chong, Y., Shvets, G., Zhang, B., 2018. Topologically protected refraction of robust kink states in valley photonic crystals. Nat. Phys. 14 (2), 140.
Grigorenko, I., Rabitz, H., 2009. Optimal control of the local electromagnetic response of nanostructured materials: optimal detectors and quantum disguises. Appl. Phys. Lett. 94 (25), 253107.
Guo, X., Zhang, W., Du, Z., 2019. Topology optimization based on explicit geometry description. Encyclopedia of Continuum Mechanics. Springer.
Guo, X., Zhang, W., Zhong, W., 2014. Doing topology optimization explicitly and geometrically new moving morphable components based framework. J. Appl. Mech. 81 (8), 81009.
Hasan, M.Z., Kane, C.L., 2010. Colloquium: topological insulators. Rev. Mod. Phys. 82 (4), 3045.
He, C., Ni, X., Ge, H., Sun, X.C., Chen, Y.B., Lu, M.H., Liu, X.P., Chen, Y.F., 2016. Acoustic topological insulator and robust one-way sound transport. Nat. Phys. 12 (12), 1124.
He, C., Yu, S.Y., Ge, H., Wang, H., Tian, Y., Zhang, H., Sun, X.C., Chen, Y., Zhou, J., Lu, M.H., et al., 2018. Three-dimensional topological acoustic crystals with pseudospin-valley coupled saddle surface states. Nat. Commun. 9 (1), 4555.
Hughes, T.J., 2012. The Finite Element Method: Linear static and dynamic finite element analysis. Courier Corporation.
Huo, S.Y., Chen, J.J., Huang, H.B., 2018. Topologically protected edge states for out-of-plane and in-plane bulk elastic waves. J. Phys.: Condens. Matter 30 (14), 145403.
Jensen, J.S., Sigmund, O., 2011. Topology optimization for nano-photonics. Laser Photon. Rev. 5 (2), 308–321.

Kang, Y., Ni, X., Cheng, X., Khanikaev, A.B., Genack, A.Z., 2018. Pseudo-spin–valley coupled edge states in a photonic topological insulator. Nat. Commun. 9 (1), 3029.
Khanikaev, A.B., Mousavi, S.H., Tse, W.K., Kargarian, M., MacDonald, A.H., Shvets, G., 2013. Photonic topological insulators. Nat. Mater. 12 (3), 233.
Kitagawa, T., Oka, T., Brataas, A., Fu, L., Demler, E., 2011. Transport properties of nonequilibrium systems under the application of light: photoinduced quantum Hall insulators without Landau levels. Phys. Rev. B 84 (23), 235108.
Kittel, C., McEuen, P., McEuen, P., 1996. Introduction to Solid State Physics. Wiley New York.
Li, W., Meng, F., Chen, Y., Li, Y.F., Huang, X., 2019. Topology optimization of photonic and phononic crystals and metamaterials: a review. Adva. Theory Simul. 1900017.
Liu, Y., Chen, X., Xu, Y., 2019. Topological phononics: from fundamental models to real materials. Adv. Funct. Mater. 1904784.
Lu, J., Qiu, C., Deng, W., Huang, X., Li, F., Zhang, F., Chen, S., Liu, Z., 2018. Valley topological phases in bilayer sonic crystals. Phys. Rev. Lett. 120 (11), 116802.
Lu, J., Qiu, C., Ke, M., Liu, Z., 2016. Valley vortex states in sonic crystals. Phys. Rev. Lett. 116 (9), 93901.
Lu, J., Qiu, C., Xu, S., Ye, Y., Ke, M., Liu, Z., 2014. Dirac cones in two-dimensional artificial crystals for classical waves. Phys. Rev. B 89 (13), 134302.
Lu, J., Qiu, C., Ye, L., Fan, X., Ke, M., Zhang, F., Liu, Z., 2017. Observation of topological valley transport of sound in sonic crystals. Nat. Phys. 13 (4), 369.
Lu, L., Joannopoulos, J.D., Soljačić, M., 2016. Topological states in photonic systems. Nat. Phys. 12 (7), 626.
Ma, G., Xiao, M., Chan, C., 2019. Topological phases in acoustic and mechanical systems. Nat. Rev. Phys. 1, 281–294.
Meeussen, A.S., Paulose, J., Vitelli, V., 2016. Geared topological metamaterials with tunable mechanical stability. Phys. Rev. X 6 (4), 41029.
Miniaci, M., Pal, R., Morvan, B., Ruzzene, M., 2018. Experimental observation of topologically protected helical edge modes in patterned elastic plates. Phys. Rev. X 8 (3), 31074.
Molesky, S., Lin, Z., Piggott, A.Y., Jin, W., Vucković, J., Rodriguez, A.W., 2018. Inverse design in nanophotonics. Nat. Photon. 12 (11), 659.
Mousavi, S.H., Khanikaev, A.B., Wang, Z., 2015. Topologically protected elastic waves in phononic metamaterials. Nat. Commun. 6, 8682.
Nanthakumar, S., Zhuang, X., Park, H.S., Nguyen, C., Chen, Y., Rabczuk, T., 2019. Inverse design of quantum spin Hall-based phononic topological insulators. J. Mech. Phys. Solid. 125, 550–571.
Nash, L.M., Kleckner, D., Read, A., Vitelli, V., Turner, A.M., Irvine, W.T., 2015. Topological mechanics of gyroscopic metamaterials. Proceed. Natl. Acad. Sci. 112 (47), 14495–14500.
Noh, J., Huang, S., Chen, K.P., Rechtsman, M.C., 2018. Observation of photonic topological valley Hall edge states. Phys. Rev. Lett. 120 (6), 63902.
Ozawa, T., Price, H.M., Amo, A., Goldman, N., Hafezi, M., Lu, L., Rechtsman, M.C., Schuster, D., Simon, J., Zilberberg, O., et al., 2019. Topological photonics. Rev. Mod. Phys. 91 (1), 15006.
Pal, R.K., Ruzzene, M., 2017. Edge waves in plates with resonators: an elastic analogue of the quantum valley Hall effect. New J. Phys. 19 (2), 25001.
Qi, X.L., Zhang, S.C., 2011. Topological insulators and superconductors. Rev. Mod. Phys. 83 (4), 1057.
Qian, K., Apigo, D.J., Prodan, C., Barlas, Y., Prodan, E., 2018. Topology of the valley-Chern effect. Phys. Rev. B 98 (15), 155138.
Rycerz, A., Tworzydło, J., Beenakker, C., 2007. Valley filter and valley valve in graphene. Nat. Phys. 3 (3), 172.
Simon, B., 1983. Holonomy, the quantum adiabatic theorem, and Berry's phase. Phys. Rev. Lett. 51 (24), 2167.
Stainko, R., Sigmund, O., 2007. Tailoring dispersion properties of photonic crystal waveguides by topology optimization. Waves Random Complex Medium 17 (4), 477–489.
Süsstrunk, R., Huber, S.D., 2015. Observation of phononic helical edge states in a mechanical topological insulator. Science 349 (6243), 47–50.
Thouless, D.J., Kohmoto, M., Nightingale, M.P., den Nijs, M., 1982. Quantized Hall conductance in a two-dimensional periodic potential. Phys. Rev. Lett. 49 (6), 405.
Vila, J., Pal, R.K., Ruzzene, M., 2017. Observation of topological valley modes in an elastic hexagonal lattice. Phys. Rev. B 96 (13), 134307.
Voon, L.C.L.Y., Willatzen, M., 2009. The kp Method: Electronic properties of semiconductors. Springer Science & Business Media.
Wang, M.Y., Wang, X., Guo, D., 2003. A level set method for structural topology optimization. Comput. Method. Appl. Mech. Eng. 192 (1–2), 227–246.
Wang, P., Lu, L., Bertoldi, K., 2015. Topological phononic crystals with one-way elastic edge waves. Phys. Rev. Lett. 115 (10), 104302.
Wang, Y.T., Luan, P.G., Zhang, S., 2015. Coriolis force induced topological order for classical mechanical vibrations. New J. Phys. 17 (7), 73031.
Wang, Z., Chong, Y., Joannopoulos, J.D., Soljačić, M., 2009. Observation of unidirectional backscattering-immune topological electromagnetic states. Nature 461 (7265), 772.
Xia, B., Wang, G., Zheng, S., 2019. Robust edge states of planar phononic crystals beyond high-symmetry points of Brillouin zones. J. Mech. Phys. Solid. 124, 471–488.
Xia, J.P., Jia, D., Sun, H.X., Yuan, S.Q., Ge, Y., Si, Q.R., Liu, X.J., 2018. Programmable coding acoustic topological insulator. Adv. Mater. 30 (46), 1805002.
Xiao, D., Chang, M.C., Niu, Q., 2010. Berry phase effects on electronic properties. Rev. Mod. Phys. 82 (3), 1959.
Xiao, D., Yao, W., Niu, Q., 2007. Valley-contrasting physics in graphene: magnetic moment and topological transport. Phys. Rev. Lett. 99 (23), 236809.
Xie, Y.M., Steven, G.P., 1993. A simple evolutionary procedure for structural optimization. Comput. Struct. 49 (5), 885–896.
Xue, R., Liu, C., Zhang, W., Zhu, Y., Tang, S., Du, Z., Guo, X., 2019. Explicit structural topology optimization under finite deformation via moving morphable void (mmv) approach. Comput. Method. Appl. Mech. Eng. 344, 798–818.
Yan, M., Lu, J., Li, F., Deng, W., Huang, X., Ma, J., Liu, Z., 2018. On-chip valley topological materials for elastic wave manipulation. Nat. Mater. 17 (11), 993.
Yu, S.Y., He, C., Wang, Z., Liu, F.K., Sun, X.C., Li, Z., Lu, H.Z., Lu, M.H., Liu, X.P., Chen, Y.F., 2018. Elastic pseudospin transport for integratable topological phononic circuits. Nat. Commun. 9 (1), 3072.
Zhang, W., Chen, J., Zhu, X., Zhou, J., Xue, D., Lei, X., Guo, X., 2017. Explicit three dimensional topology optimization via moving morphable void (mmv) approach. Comput. Method. Appl. Mech. Eng. 322, 590–614.
Zhang, W., Yang, W., Zhou, J., Li, D., Guo, X., 2017. Structural topology optimization through explicit boundary evolution. J. Appl. Mech. 84 (1), 11011.
Zhang, W., Yuan, J., Zhang, J., Guo, X., 2016. A new topology optimization approach based on moving morphable components (mmc) and the ersatz material model. Struct. Multidiscip. Optim. 53 (6), 1243–1260.
Zhang, Z., Tian, Y., Wang, Y., Gao, S., Cheng, Y., Liu, X., Christensen, J., 2018. Directional acoustic antennas based on valley-Hall topological insulators. Adv. Mater. 30 (36), 1803229.